X-ray phase radiography and tomography with grating interferometry and the reverse
projection technique

X-ray phase radiography and tomography with grating interferometry and the reverse projection technique

Zhili Wang[1], Kun Gao[1], Xin Ge[1], Zhao Wu[1], Heng Chen[1], Shenghao Wang[1], Peiping Zhu[2], Qingxi Yuan[2], Wanxia Huang[2], Kai Zhang[2] and Ziyu Wu[1,2,3]

[1] National Synchrotron Radiation Laboratory, University of Science and Technology of China, Hefei 230026, People's Republic of China
[2] Institute of High Energy Physics, Chinese Academy of Sciences, Beijing 100049, People's Republic of China

E-mail: wuzy@ustc.edu.cn

Abstract

X-ray grating interferometry provides substantially increased contrast over conventional absorption-based imaging methods, and therefore new and complementary information. Compared with other phase-contrast imaging techniques, x-ray grating interferometry can overcome some of the problems that have impaired the applications of x-ray phase-contrast radiography and phase tomography. Recently, special attention has been paid to the development of quantitative phase retrieval methods, which is mandatory to perform x-ray phase tomography, to achieve material identification, to differentiate distinct tissues, etc. Typically, the phase-stepping approach has been utilized for phase retrieval in grating interferometry. This method requires a grating scanning and acquisition of multiple radiographic projections, and therefore is disadvantageous in terms of imaging speed and radiation damage. Here we present an innovative, highly sensitive approach, dubbed 'reverse projection' (RP), for quantitative phase retrieval. Compared with the phase-stepping approach, the present RP method abandons grating scanning completely, and thus is advantageous due to its much higher efficiency and the reduced radiation dose, without the degradation of reconstruction quality. This review presents a detailed explanation of the principle of the RP method. Both radiography and phase tomography experiments are performed to validate the RP method. We believe that this new technique will find widespread applications in biomedical imaging and *in vivo* studies.

(Some figures may appear in colour only in the online journal)

1. Introduction

Over the last couple of decades, x-ray phase-contrast imaging (PCI) has been attracting increasing attention. This technique is intrinsically capable of providing phase information of the investigated object, and therefore potentially revolutionizes conventional x-ray radiologic approaches. For negligible anisotropy in the medium, the complex refractive index characterizing the optical properties of an object can be written as $n = 1 - \delta + i\beta$, with the decrement of the real part δ responsible for the phase shift, and the imaginary part β describing the attenuation properties. In conventional x-ray radiography, the image contrast is obtained through the differences in the attenuation properties of the materials, and the phase shift information is lost. However, for those soft tissues and at diagnostically relevant photon energies, the phase shift plays a more prominent role than the attenuation because δ is typically three orders of magnitude greater than β (Momose and Fukuda 1995). Therefore, phase-contrast techniques are expected to yield significantly improved image contrast when compared with conventional attenuation-based

[3] Author to whom any correspondence should be addressed.

modalities. Furthermore, the dependence on the photon energy is weaker for δ than for β. As a consequence, phase signals are expected to be obtained with much lower dose deposition than attenuation, which is an issue of great importance when radiation damage has to be considered.

Over the last few decades, various techniques have been developed to probe phase variations induced by a sample. They can be classified into crystal interferometric methods (Bonse and Hart 1965, Momose *et al* 1996), propagation-based imaging (PBI) methods (Snigirev *et al* 1995, Nugent *et al* 1996, Wilkins *et al* 1996), analyser-based imaging (ABI) methods (Davis *et al* 1995, Chapman *et al* 1997, Zhu *et al* 2005, 2006), grating interferometric (GI) (David *et al* 2002, Momose *et al* 2003, Pfeiffer *et al* 2006a, Zhu *et al* 2010) and grating non-interferometric methods (Olivo and Speller 2007, Huang *et al* 2009). These methods differ vastly in the nature of the recorded signal, the experimental set-up, the requirements on the illuminating radiation (especially its spatial coherence and monochromaticity), and the amount of radiation dose imparted to the sample.

X-ray grating interferometry (GI) is based on the fractional Talbot effect discovered over one hundred years ago (Talbot 1836). Since its feasibility first demonstrated about one decade ago (David *et al* 2002, Momose *et al* 2003), x-ray GI has become a widely used PCI technique (Weitkmap *et al* 2005, McDonald *et al* 2009, Momose *et al* 2009). The development of GI has been performed mainly using synchrotron radiation sources. Microfocus x-ray tubes can also provide sufficient spatial coherence for the image formation, but the available flux is quite low, leading to long exposure times. Recently, Pfeiffer *et al* (2006a) demonstrated the feasibility of Talbot–Lau interferometry in the hard x-ray region, where low-brilliance x-ray tubes were efficiently used to produce quantitative phase images. This was considered a breakthrough in x-ray imaging since, for the first time, it was shown that PCI can be efficiently performed with conventional tube sources. Additionally, an x-ray grating interferometer is easy to align, and can be scaled up to large fields of view (McDonald *et al* 2009). All of these characteristics make x-ray GI superior to other phase-contrast techniques and set the pre-requisites for widespread applications of x-ray phase-contrast radiography and tomography. Some alternative experimental set-ups have also been proposed (Takeda *et al* 2007, Nesterets and Wilkins 2008, Huang *et al* 2009, Krejci *et al* 2010, Du *et al* 2011). Theoretical analysis has been presented on the effects of partial spatial coherence and polychromaticity on the performance of GI (Weitkamp *et al* 2006, Wang *et al* 2010a, 2010b, 2010c, Ge *et al* 2011).

Preclinical studies have shown great potential for a variety of imaging applications and prove the clinical significance of GI. PCI of the breast has been one of the first medical applications of x-ray PCI (Arfelli *et al* 1998, Pisano *et al* 2000). Stampanoni *et al* (2011) presented the first *ex vivo* images of fresh, native breast tissue using a grating interferometer and a conventional x-ray tube. GI yielded improved diagnostic capabilities especially in discerning the type of malignant conversions and their breadth within normal breast tissue. In the field of musculoskeletal PCI, *ex vivo* GI images of

an infant hand showed that tendons and ligaments appeared with strongly increased contrast-to-noise ratio when compared with absorption contrast images (Donath *et al* 2010). Images of a cadaveric human finger using conventional x-ray tubes showed that the refraction contrast was dominated by tendon embedded in muscle, with the cartilage layer difficult to be recognized (Stutman *et al* 2011). Nevertheless, the joint model of the hand predicted that a GI radiographic system could be feasible under optimized experimental conditions. With respect to potential applications of x-ray GI for neuroimaging, *in vitro* GI tomographic images of a tumour-bearing rat brain clearly depicted the tumour tissue and the white and grey matter in a cerebellum (Pfeiffer *et al* 2007). McDonald *et al* (2009) presented GI images of a healthy rat brain, where the hippocampus and *substantia nigra* structure were clearly observed with an increased sensitivity. Applied to human cerebellum, GI allowed the identification of the blood vessels, the stratum moleculare, the stratum granulosum and the white matter (Schulz *et al* 2010). Furthermore, proof-of-principle studies with GI in micro-CT mode were performed on the brains of AD-model mice, demonstrating its ability in visualizing the amyloid plaques in the cortex and hippocampus of the brain (Pinzer *et al* 2012). These pioneering results already demonstrate that x-ray GI indeed provides an increased sensitivity and improved diagnostic performance in radiography and/or computed tomography. A preclinical x-ray phase-contrast CT scanner has been developed by Tapfer *et al* (2012), which represents a milestone in translating x-ray PCI from proof-of-principle experiments to preclinical imaging applications, and might accelerate the implementation of x-ray GI to currently existing medical imaging systems.

For a quantitative determination of the GI phase sensitivity, the signal and noise properties have been investigated. In radiography, Revol *et al* (2010) presented quantitative descriptions for the stochastic error of grating-based differential phase contrast (DPC) imaging using the error propagation formula. Modregger *et al* (2011) developed a numerical framework for a realistic and quantitative determination of the sensitivity of GI. The covariance matrices of the absorption, differential phase/refraction and scattering images in GI have also been calculated using a least-squares fitting algorithm (Weber *et al* 2011). In phase computed tomography (PCT), the noise power spectrum (NPS) of grating-based x-ray phase-contrast computed tomography is investigated and compared with that of the conventional CT (Kohler *et al* 2011, Tang *et al* 2011). Chen *et al* (2011) derived the noise variance versus spatial resolution relationship in DPC projection imaging and CT, and compared with conventional absorption-based x-ray projection imaging and CT.

In one-dimensional (1D) GI, the phase and absorption gratings are both periodic in one direction. Therefore, the interferometer shows lack of sensitivity to object structures oriented perpendicularly to the grating lines. This may result in artefacts in the retrieved phase image from 1D differential phase image (Kottler *et al* 2007). To overcome the disadvantages of 1D GI, two-dimensional (2D) grating interferometers have been developed using either two closely
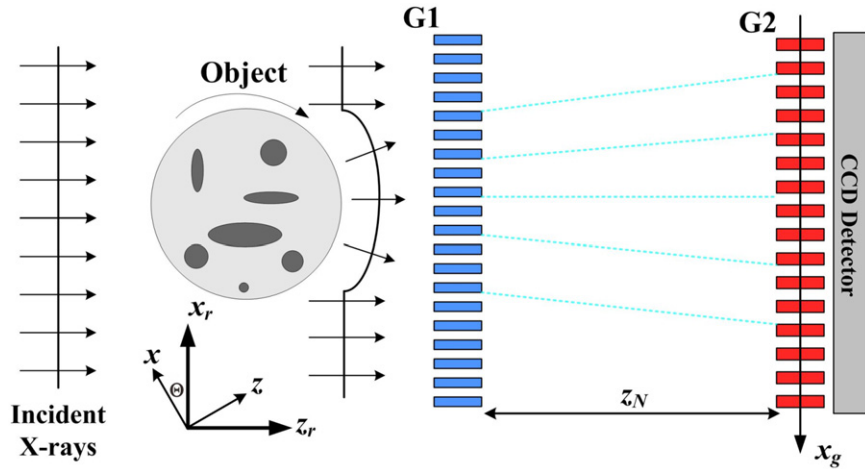
Figure 1. Layout of 1D x-ray GI. An interference fringe pattern is formed downstream the phase grating G1, and is locally distorted by the sample placed in the beam. The analyser grating G2 converts the pattern distortion into intensity variations recorded by the CCD detector.

stacked 1D gratings (Zanette *et al* 2010) or genuine 2D chess-board gratings (Itoh *et al* 2011). 2D Talbot–Lau interferometers have also been introduced to apply 2D GI for laboratory use (Sato *et al* 2011). Absorption, refraction and scattering images were obtained by Fourier analysis of a single Moiré fringe pattern. 2D phase grating has also been used together with a high-resolution detector without the absorption grating (Rizzi *et al* 2011). 2D differential phase CT images can also be obtained by slightly tilting the gratings with respect to the rotation axis of the object (Rutishauser *et al* 2011a). 2D GI has been applied to x-ray optics metrology, including characterization of refractive x-ray lenses (Rutishauser *et al* 2011b), and wavefront measurements of hard x-ray free-electron lasers (Rutishauser *et al* 2012). The combination of a 2D grating interferometer with a Fresnel zone plate allows quantitative submicrometer PCI (Berujon *et al* 2012).

In the past decades, several approaches have been proposed for quantitative phase retrieval, which is mandatory to perform x-ray phase tomography, to discriminate different types of tissues and so on. Among them, the phase-stepping (PS) technique is most frequently used (Weitkamp *et al* 2005). This technique requires transverse scanning one of the gratings by a fractional distance of the grating period, and acquisition of multiple images at these scan points. The attenuation, refraction (i.e. differential phase) and scattering images can be extracted simultaneously from the acquired image series using fast Fourier transform. However, the PS approach has two major drawbacks. One is its poor time resolution, resulting from the fact that the sample is supposed to be static during PS. The even more critical one is that the PS method necessarily requires the acquisition of at least three images. Therefore, avoiding PS and acquisition of multiple images would increase the imaging speed significantly, especially in x-ray phase tomography.

Another approach for phase retrieval is the Fourier transform method. A Fourier analysis of the Moiré fringe pattern produces the absorption, refraction and scattering images from a single exposure (Takeda *et al* 1982). Therefore, the method abandons the time-consuming grating scanning procedure, and is advantageous in reduced exposure times

and high imaging speed. With the use of white synchrotron radiation, Momose *et al* (2009) demonstrated high-speed x-ray phase imaging and tomography, and time-resolved four-dimensional (4D) x-ray phase tomography for dynamic observation of a living worm (Momose *et al* 2011). CT images of absorption, refraction and scattering are obtained using a Talbot–Lau interferometer without PS (Bevins *et al* 2012). Compared with the PS method, the disadvantage of the Fourier transform method is the degraded spatial resolution, resulting in anisotropic pixels in the retrieved projections and anisotropic voxels in the reconstructions (Bevins *et al* 2012).

In the following, we propose an alternative approach, dubbed 'reverse projection' (RP), which can retrieve the phase information without grating scanning. The strength of the presented RP method is based on a novel manipulation of the phase relation between different x-ray projections. With respect to the PS technique, the RP method does not require any further constraints, thus removing the mentioned two major limitations of the PS technique. In this review, we present a detailed explanation of the principle of the RP method. The concept of shifting curve (SC) is introduced to describe the measured intensity as a function of the grating position. With the grating interferometer tuned to the slope position of the SC, the refraction is linear with small intensity changes. Based on this linear behaviour, a novel phase retrieval technique, named the 'reverse projection' (RP) method, is derived by the use of the phase relation between different x-ray projections. Radiography and phase tomography experiments are performed to validate the RP method. Finally, the extension of the RP method to fan beam illumination is discussed.

2. Theory and methods

2.1. The shifting curve

Consider the imaging set-up schematically presented in figure 1, which consists of an x-ray source, a phase grating (G1), an analyser absorption grating (G2) and an image detector. The inter-grating distance is set to one of the fractional Talbot distances of G1, denoted by z_N, so that the

self-image of G1 is formed on G2. When a sample is placed immediately in front of G1, the self-image is deformed due to the x-ray refraction induced by the sample. The analyser grating G2 transforms the deformation into intensity variations recorded by the detector placed just behind G2. Here, the optical axis is parallel to the z-axis, and the line pattern of the gratings is parallel to the y-axis.

Consider the situation where the phase grating G1 is illuminated with coherent unit-amplitude plane-wave x-rays of wavelength λ. The complex transmission function $t(x)$ of G1 is expressed as a Fourier series (Momose *et al* 2003)

$$t(x) = \sum_n \alpha_n \exp\left(2\pi i \frac{nx}{p_1}\right) \tag{1}$$

where α_n and p_1 are the amplitude of the nth harmonic and the period of G1, respectively. Under paraxial approximation, the wave field at fractional Talbot distances z_N is given by

$$E(x, z_N) = \sum_n \beta_n(z_N) \exp\left(2\pi i \frac{nx}{p_1}\right) \tag{2}$$

with $\beta_n(z_N) \equiv \alpha_n \exp(-i\pi\lambda z_N n^2/p_1^2)$. The intensity of the interference fringe pattern is given by

$$I_s(x, z_N) = |E(x, z_N)|^2 = \sum_n a_n(z_N) \exp\left(2\pi i \frac{nx}{p_1/\eta}\right) \tag{3}$$

where

$$a_n(z_N) \equiv \sum_m \beta_{n\eta+m}(z_N)\beta_m^*(z_N). \tag{4}$$

For monochromatic plane waves, i.e. in the parallel beam case, the maximum contrast of the fringes is achieved at fractional Talbot distances z_N:

$$z_N = N \frac{p_1^2}{2\eta^2\lambda} \tag{5}$$

where $N = 0, 1, 2, \ldots$ is an integer number called the Talbot order. The factor η, depending on the type of G1, satisfies $\eta = 1$ for a $\pi/2$-shifting phase grating or an amplitude grating, and $\eta = 2$ for a π-shifting phase grating. The maximum contrast of intensity modulation is achieved for an absorption grating at even Talbot orders ($N = 0, 2, 4, \ldots$) and for a phase grating at odd Talbot orders ($N = 1, 3, 5, \ldots$) (Suleski 1997).

For spherical waves, i.e. in cone beam geometry, the fractional Talbot distances rescale according to the Fresnel scaling theorem as

$$D_N = \frac{L}{L - z_N} z_N \tag{6}$$

with L being the distance between the source and G1.

Since the period of the fringes is too small to be resolved directly, an absorption grating G2 is employed, as illustrated in figure 1. The transmittance function $T(x)$ of the analyser grating G2, with the same pitch as that of the interference fringes, is given by (Momose *et al* 2003)

$$T(x) = \sum_n b_n \exp\left(2\pi i \frac{nx}{p_1/\eta}\right) \tag{7}$$

with b_n being the amplitude of the nth harmonic. And then, the intensity recorded by the image detector is given by

$$I(x_g, z_N) = I_s(x, z_N) \otimes T(x) = \sum_n a_n b_n \exp\left(2\pi i \frac{nx_g}{p_1/\eta}\right) \tag{8}$$

where $\otimes$ denotes a 1D convolution operation, and x_g is the relative shift of G2 against the self-image of G1 in the x direction. Note that the factor describing the contrast with the period p_1/η has been averaged out in equation (8). As revealed by equation (8), the measured intensity in GI varies as a function of the relative shift x_g. We note that this case is quite similar to that of ABI. In ABI, the measured intensity is strongly dependent on the relative angle between the two crystals. And this relationship is described by the rocking curve (RC) (Zachariasen 1945). In analogy to the RC, here we introduce the concept of SC to describe the recorded intensity as a function of the relative shift x_g (Zhu *et al* 2010):

$$S(x_g, z_N) \equiv \sum_n a_n b_n \exp\left(2\pi i \frac{nx_g}{p_1/\eta}\right). \tag{9}$$

As an example, figure 2(*a*) shows the SC for a $\pi/2$ phase grating at the first fractional Talbot distance. By use of SC, the recorded intensity in GI can be generally written as

$$I(x_g, z_N) = I_0 S(x_g, z_N) \tag{10}$$

with I_0 being the x-ray intensity incident on G1.

2.2. The RP method

When an object is placed just before G1, the interference pattern is locally distorted from its reference shape, and the measured intensity varies correspondingly. Relying on the physical similarities between ABI and GI, the intensity recorded by the detector can be expressed as (Zhu *et al* 2010)

$$I(x_r, y) = I_0 \exp(-M) \cdot S(x_g + z_N\theta) \tag{11}$$

where $M(x_r, y) = \int \mu(x, y, z) \, dz_r$ represents the object's absorption with μ the linear absorption coefficient; $S(x_g)$ is the SC, and θ is the refraction angle in the plane perpendicular to the grating lines (X–Z plane), and determined by (Born and Wolf 1999)

$$\theta(x_r, y) = -\frac{\lambda}{2\pi} \frac{\partial \Phi(x_r, y)}{\partial x_r} = -\int \frac{\partial \delta(x, y, z)}{\partial x_r} \, dz_r \tag{12}$$

where $\Phi(x_r, y)$ is the phase shift.

As shown in figure 2(*b*), the derivative of the SC is fairly constant at its half-slopes, i.e. $x_g^l = -p_1/4\eta$ (left half-slope) or $x_g^r = p_1/4\eta$ (right half-slope), as indicated by the arrows in figure 2(*a*). Therefore, the behaviour of the SC near its half-slope can be considered linear with a good approximation. For small values of θ satisfying $|\theta| \leqslant p_1/(4\eta z_N)$, $S(x_g^r + z_N\theta)$ can be replaced by its first-order Taylor expansion around the half-slope position:

$$S(x_g^r + z_N\theta) = S(x_g^r) + \frac{dS(x_g^r)}{dx_g} z_N\theta = S(x_g^r)(1 + C\theta) \tag{13}$$

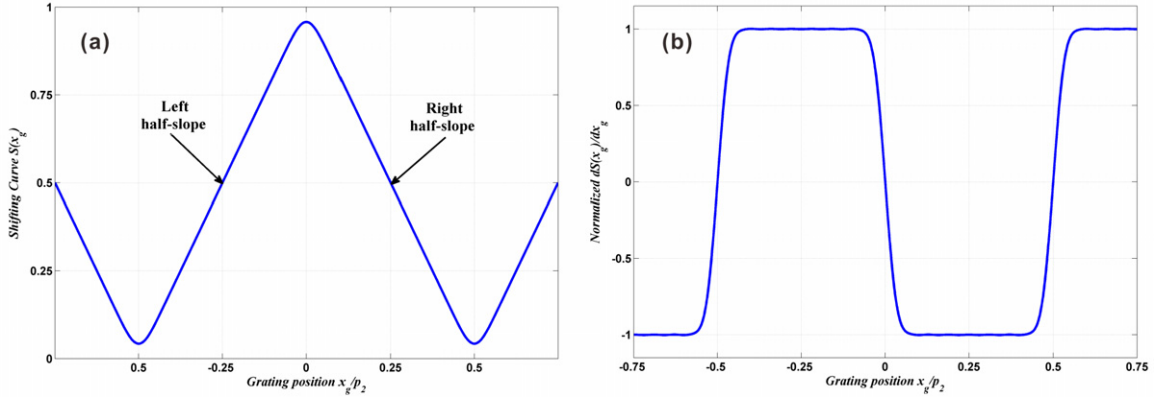**Figure 2.** Plot of the SC (*a*) and its normalized derivative (*b*) as a function of x_g in units of the analyser grating period. A $\pi/2$-shifting phase grating and monochromatic illumination at 25 keV are assumed. The spatial coherence length is three times of the self-image period.

where

$$C = \left[z_N \frac{dS(x_g^r)}{dx_g} \right] / S(x_g^r). \quad (14)$$

On substitution of equations (12) and (13) into equation (11), the intensity of the projected image in GI can be written as

$$I(x_r, z_N) = I_0 \exp\left[-\int \mu(x, y, z)\, dy_r \right] \cdot S(x_g^r)[1 + C\theta]. \quad (15)$$

As shown in figure 1, two reference frames are introduced here: the coordinates (x_r, y, z_r) represent the reference frame associated with the x-ray beam, while (x, y, z) that associated with the object. These two frames are linked by a rotation matrix (Zhu *et al* 2010):

$$\begin{pmatrix} x \\ z \end{pmatrix} = \begin{pmatrix} \cos\Theta & -\sin\Theta \\ \sin\Theta & \cos\Theta \end{pmatrix} \begin{pmatrix} x_r \\ z_r \end{pmatrix} \quad (16)$$

with Θ being the rotation angle from the x_r-axis to the x-axis around the y-axis.

The first projection image is acquired at the rotation angle Θ, and the second image has the x-axis of the object frame inverted, i.e. at the rotation angle $\Theta + \pi$. The inversion of the z-axis does not matter since we are dealing with projection images along the z direction. The transformation of the two images from the beam frame to the object frame leads to

$$M(\Theta + \pi) = M(\Theta) \quad \theta(\Theta + \pi) = -\theta(\Theta). \quad (17)$$

Note that the absorption image M remains the same, while the refraction angle undergoes a change of sign in the transformation. This can be understood in terms of the spatial gradient of the refractive index along the x direction. An inversion of x changes the algebraic sign of the refraction angle. Combining equations (15) and (17), the projection images recorded at the rotation angle Θ and its corresponding RP image at $\Theta + \pi$ can be written as

$$I(x_r, \Theta, y) = I_0 \exp\left[-\int \mu(x, y, z)\, dy_r \right] \cdot S(x_g^r)[1 + C\theta] \quad (18)$$

$$I(-x_r, \Theta + \pi, y) = I_0 \exp\left[-\int \mu(x, y, z)\, dz_r \right] \\ \times S(x_g^r)[1 - C\theta]. \quad (19)$$
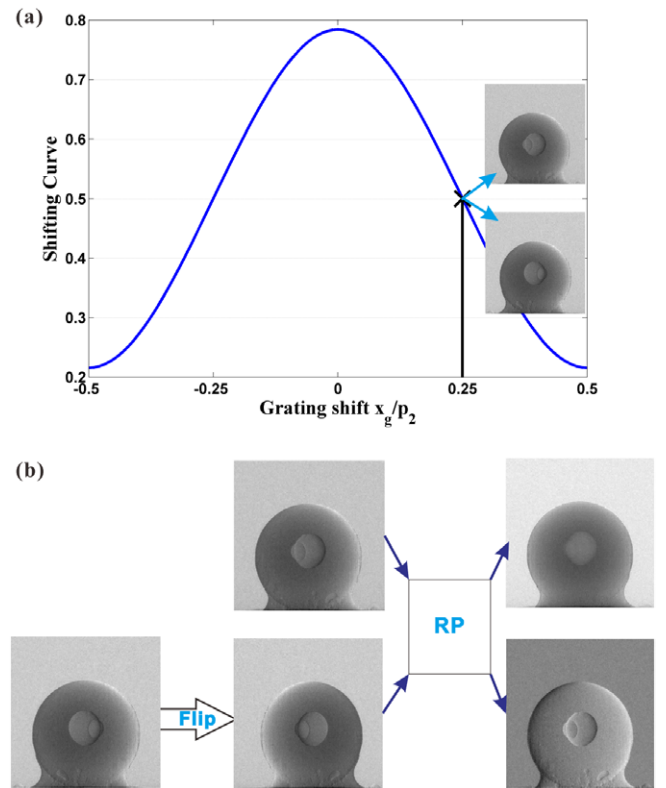

Figure 3. Grating setting, acquired images and image analysis of the RP method: (*a*) calculated SC for the given experimental parameters. A grating setting at the right half-slope $x_g^r = p_2/4$ is shown together with the acquired images. (*b*) Inversion process of the RP image and subsequent analysis leading to the absorption image M and the refraction angle image θ.

Consequently, the absorption image can be obtained from the two projection images by the sum of equations (18) and (19),

$$M(x_r, \Theta, y) = \ln\left[\frac{2S(x_g^r)I_0}{I(x_r, \Theta, y) + I(-x_r, \Theta + \pi, y)} \right] \quad (20)$$

and the refraction angle image is obtained by a proper combination of equations (18) and (19),

$$\theta(x_r, \Theta, y) = \frac{1}{C} \frac{I(x_r, \Theta, y) - I(-x_r, \Theta + \pi, y)}{I(x_r, \Theta, y) + I(-x_r, \Theta + \pi, y)}. \quad (21)$$
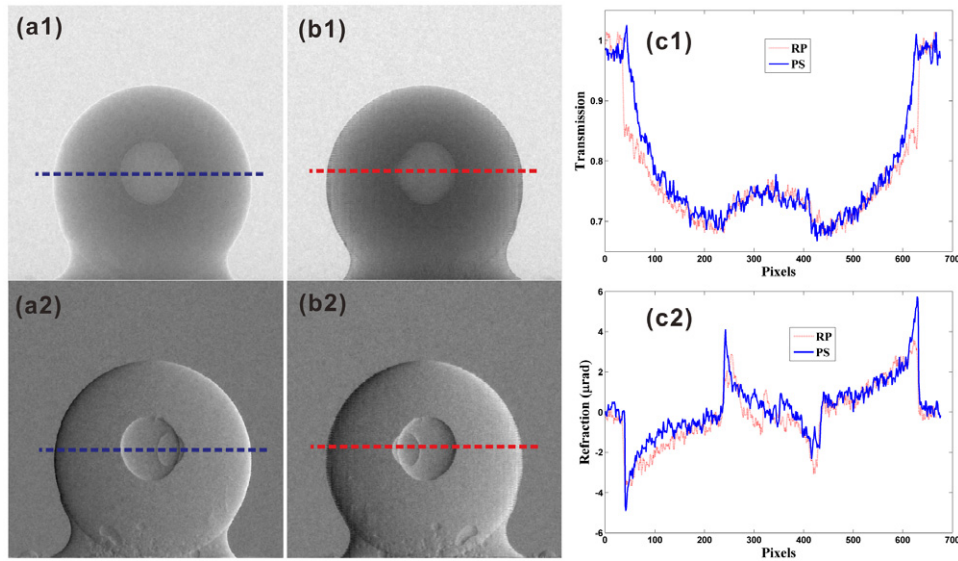
Figure 4. Analysis of the retrieved absorption and refraction angle images: (*a*1), (*a*2) absorption and refraction angle images obtained by the five-step PS method; (*b*1), (*b*2) absorption and refraction angle images obtained by the RP method; (*c*1), (*c*2) Line profiles from the absorption and refraction angle images, respectively, as indicated by the horizontal lines.

Furthermore, the phase shift of the object $\Phi(x_r, y)$ can be retrieved from the refraction angle $\theta(x_r, \Theta, y)$. This yields the complete knowledge of the object's complex transmission function.

Based on equations (20) and (21), we introduce here an original acquisition protocol, dubbed the 'reverse projection' (RP) method. The RP method is applied on a pixel-by-pixel basis to the acquired two projection images. With no object in the beam, we scan one of the gratings along the transverse direction over one grating period and record the normalized intensity I/I_0 on the detector versus the transverse shift x_g. Actually, we collect the SC $S(x_g)$ and then set the grating interferometer at the centre of the linear region of the SC. With object placed before G1, two projection images are acquired. The object absorption and refraction angle images are then retrieved using equations (20) and (21), respectively. We have performed both radiography and tomography experiments to validate the RP method. And the results are shown in section 3.

3. Experimental results

3.1. 2D Radiography

Radiography experiments were performed at the Department of Advanced Materials Science of the Graduate School of Frontier Sciences, University of Tokyo. We used an x-ray tube with a tungsten target operated at 50 kV/120 μA, with a focal spot size of 8 μm (L9181S, Hamamatsu Photonics K.K.). The grating G1 is a $\pi/2$-shifting phase grating for a mean photon energy of 25 keV with a pitch of 4.5 μm, and the absorption grating G2 with a pitch of 5.3 μm is placed 60 mm upstream of the detector. The test object used to assess the RP method was a polyoxymethylene (POM) sphere with a diameter of 7.9 mm, located 90 mm upstream of G1. The detector involved in the experiment is a fibre-coupled charged coupled device (CCD) with $4k \times 4k$ pixels and an effective pixel size of 18 μm. The

source-to-G1 distance is 1340 mm, and the G1-to-G2 distance is 240 mm, i.e. the first fractional Talbot distance. Under the above conditions, the measured visibility of the Moiré fringe was about 35%. For comparison, a PS approach with five steps was also performed, and its results served as the reference.

Figure 3 shows the grating setting, the acquired radiographic images and image analysis of the RP method. Figure 3(*a*) shows the calculated SC according to the above experimental parameters. The grating setting at the right half-slope $x_g^r = p_2/4$ is shown along with the two acquired images. Figure 3(*b*) shows the process of the inversion of the RP image and subsequent analysis, which leads to the absorption image M and the refraction angle image θ.

Figure 4 shows the retrieval results of the RP and the five-step PS methods. Figures 4(*a*1) and (*b*1) show the absorption images obtained by the PS method and the RP method, respectively, while figures 4(*a*2) and (*b*2) show the corresponding refraction angle images. Line profiles horizontally across the test object are also shown in figures 4(*c*1) and (*c*2) for the absorption and the refraction angle images, respectively, for a quantitative comparison. As can be seen, good agreement is obtained for all those cases.

As demonstrated in figure 4, the proposed RP method indeed provides quantitative information retrieval with only two projection images collected at two reverse viewing angles. Compared with the PS technique, the RP method completely abandons the time-consuming grating scanning procedure, and yields comparable results with a significantly reduced exposure time and radiation dose. Therefore, we can expect that the RP method is a good candidate for future time-resolved dynamic observation of weakly absorbing objects (Momose *et al* 2009, 2011), such as soft materials and biological specimens.

3.2. 3D phase tomography

As shown in equation (12), the refraction angle is determined by the line integral of the first-order spatial derivative

Table 1. Experimental parameters for the phase tomography of the three investigated specimens.

	Mouse joint		Rat brain		Rat paw	
	PS	RP	PS	RP	PS	RP
Rotation (°)	0–180	0–360	0–180	0–360	0–180	0–360
Pixel size (μm)	3.5×3.5	3.5×3.5	11.2×11.2	11.2×11.2	7.4×7.4	7.4×7.4
Field of view (mm)	3.58×3.58	3.58×3.58	11.45×3.6	11.45×3.6	15.5×3.6	15.5×3.6
Number of projections	181	361	361	721	501	1001
Phase steps	9	1	9	1	9	1
Single exposure (ms)	200	200	200	200	60	60
Total exposure (s)	326	72	650	144	270	60
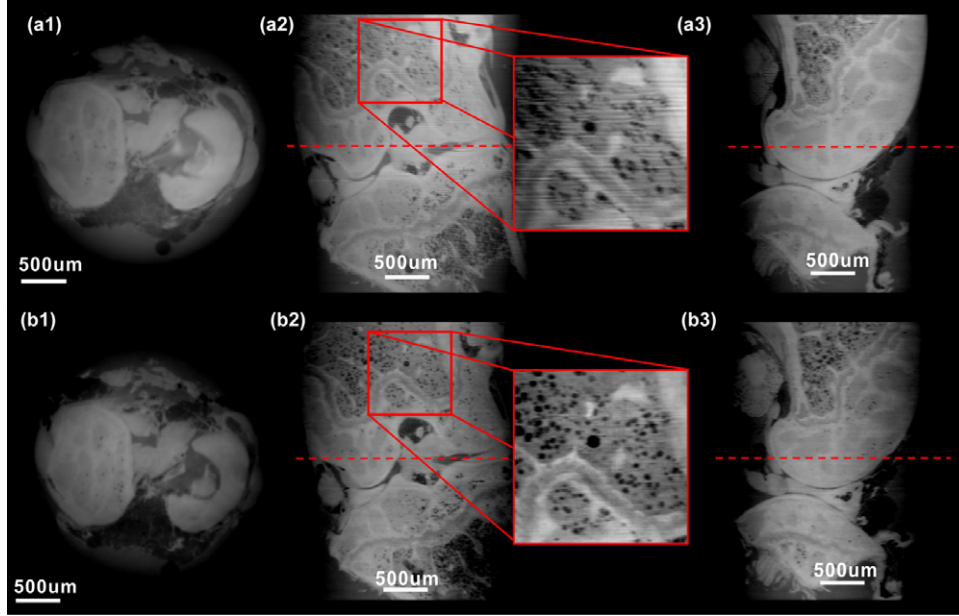
Figure 5. Tomographic reconstructions of a demineralized mouse joint. (a1)–(a3) show the reconstructions obtained with the PS technique, and (b1)–(b3) the results by the RP method. (a1) and (b1) show an axial slice, (a2) and (b2) depict a coronal slice, and (a3) and (b3) show a sagittal view through the joint. The dotted lines mark the locations where the axial views were taken (Zhu *et al* 2010).

of the refractive index decrement along the beam path. Therefore, if refraction angles are measured from multiple angular directions, a 3D distribution of $\delta(x, y, z)$ can be reconstructed by applying the algorithm of computed tomography (CT), i.e. phase tomography. Specifically, the linear absorption coefficient and the refractive index decrement can be determined by the inverse Fourier transform and a Hilbert transform, respectively:

$$\mu(x, y, z) = \int_0^\pi d\Theta \int_{-\infty}^\infty [M(x_r, \Theta, y)$$
$$\times F^{-1}(|\rho|)] \cdot \delta(x \cos \Theta + y \sin \Theta - x_r) \, dx_r \quad (22)$$

$$\delta(x, y, z) = -\int_0^\pi d\Theta \int_{-\infty}^\infty [\theta(x_r, \Theta, y)$$
$$\times F^{-1}(|\rho|/2\pi j\rho)] \cdot \delta(x \cos \Theta + y \sin \Theta - x_r) \, dx_r \quad (23)$$

where F^{-1} denotes the inverse Fourier transform, ρ is the spatial frequency and $\delta(\cdot)$ is the Dirac delta function.

In phase tomography, the experimental procedure of the RP method can be described in the following steps:

(i) place the investigated object immediately in front of the phase grating and record m angular projections during an object rotation of 360°;

(ii) retrieve the absorption signal M and the refraction angle θ according to equations (20) and (21), respectively;

(iii) reconstruct the linear absorption coefficient and/or the refractive index decrement by use of equations (22) and/or (23), respectively. Therefore, the total number of acquired angular projections is m.

Compared with the PS method, the total number of acquired projections in the RP method is reduced by a factor of $n/2$, with n being the number of phase steps per projection. Although the noise from photon statistics is reduced by averaging multiple images in the PS protocol, the mechanical drift induced by the grating scanning procedure is increased, resulting in a degradation of the retrieved image quality. We performed PS and RP experiments at the TOMCAT beamline of the Swiss Light Source at the Paul Scherrer Institut (Stampanoni *et al* 2006), to validate the proposed RP method. More details about the interferometer are described by McDonald *et al* (2009).

In the first study, two distinct samples were investigated. One is a rat brain first fixed in paraformaldehyde (PFA) and then embedded in paraffin, and the other a demineralized mouse joint fixed in phosphate buffer solution (PBS). These two weakly absorbing specimens are ideal candidates for x-ray PCI. The rat brain and the mouse joint were used to test the

reconstruction method on large ($>10\,\mathrm{mm}$) and small ($<4\,\mathrm{mm}$) specimens, respectively. Table 1 summarizes the experimental parameters for the PS and RP methods, and figures 5 and 6 show the reconstruction results using the two methods, respectively.

Figure 5 shows axial, sagittal and coronal views of a mouse joint obtained with the PS and RP approaches. To avoid any movement artefacts, the joint was immersed and fixed in PBS during the tomographic scan. It is clearly shown that, from a qualitative comparison of the corresponding views, the RP reconstructions are indeed comparable to those obtained with the PS method. Furthermore, the insets shown in figures 5(*a*2) and (*b*2) reveal that the RP-reconstructed slice appears to be sharper than that of the PS approach, and is less sensitive to typical horizontal stripe artefacts observed with the PS method. This can be explained as follows. In the RP protocol, the grating interferometer is set to the slope position of the SC. And then the refraction angle is proportional to the small intensity variations, and is obtained by a simple subtraction of a reference image from the paired images described by equation (21). Additionally, no grating scanning is performed in the RP method, and thus the reconstruction slices contain no error due to mechanical drifts. However, a careful analysis of the reconstructed slices points out that the RP protocol requires a better uniformity and lower local imperfections within the field of view than the PS method. These grating defects could result in small ring-like artefacts in the RP reconstructions which are not so evident in the PS-reconstructed slices. A more detailed analysis of this issue will be presented in section 4.

As a representative of large specimens, a rat brain was investigated to test the RP method. The rat brain was vertically on the sample support, to match the horizontal field of view of the imaging system. Additional benefit of the vertical sample configuration is that it enables a direct reconstruction of coronal slices through the sample, a very useful approach when trying to identify anatomical brain regions (Pfeiffer *et al* 2007). Four scans were acquired along the vertical direction of the beam to image the whole brain. Scanning was performed in an aquarium bath filled with liquid paraffin, to avoid phase-wrapping and beam-hardening effects. A qualitative comparison of figures 6(*a*) and (*b*) reveals that for large samples, the RP reconstruction is also comparable to the PS reconstruction. Additionally, figure 6(*c*) shows a quantitative comparison of line profiles extracted at the hippocampus region between the RP and PS reconstructions. The good agreement between the results of the RP and PS approaches confirms the validity of the RP method.

In the second study, we tested the proposed RP method using a more realistic specimen containing hard and soft tissues simultaneously. For this purpose, we studied a rat paw fixed in PFA, which contained both muscles and bones. The rat paw was vertically mounted to match the field of view of the imaging system. Seven stacked scans were stitched to cover the whole sample.

As the most challenging experiment, the rat paw was mostly measured in air. This usually leads to the phase-wrapping phenomenon between the specimen and the surrounding air. In figure 7(*b*1), visible 'star' artefacts were
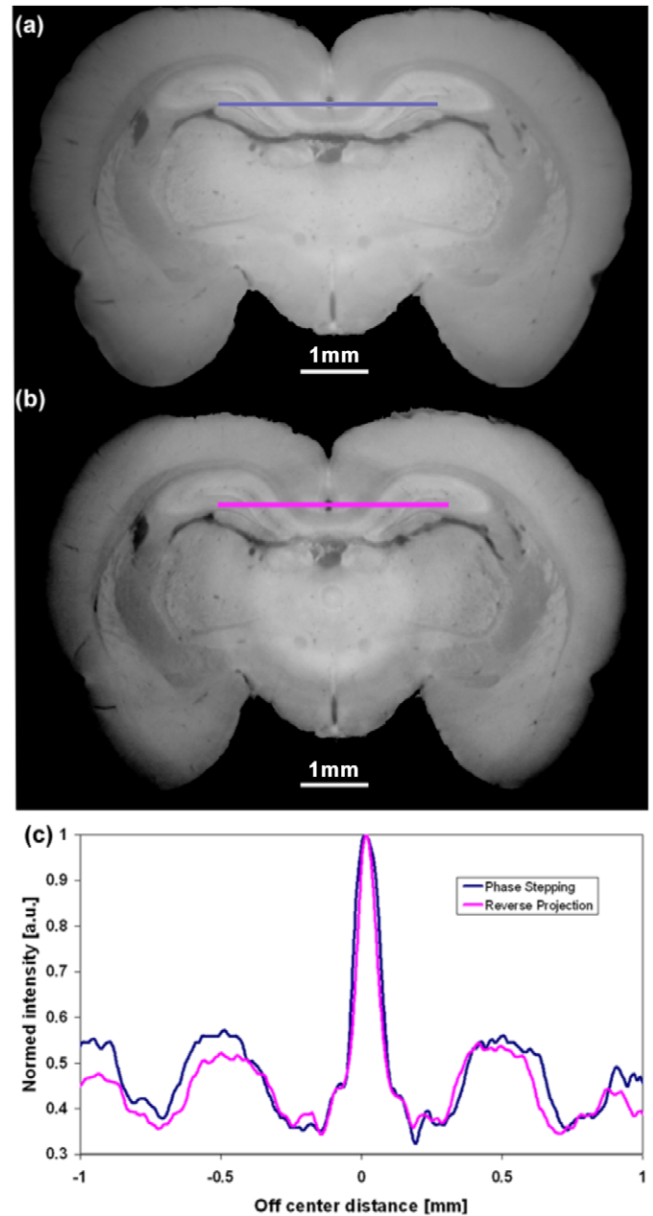

Figure 6. Coronal slices of a rat brain, obtained after tomographic reconstructions using the PS (*a*) and RP (*b*) approach, respectively. The plot in (*c*) shows a quantitative comparison between two line profiles taken at the hippocampus region (Zhu *et al* 2010).

observed, which can be attributed to the phase-wrapping, while in figure 7(*c*1) those artefacts are less serious. This can be explained as follows. When the refraction angle exceeds the linear region, i.e. $\theta \geqslant p_2/4z_N$, the SC is saturated. And consequently, the RP method is not sensitive to such large refraction angles. In contrast, refraction angles satisfying $\theta \leqslant p_2/(2z_N)$ can be quantitatively retrieved by the PS method.

In conclusion, the presented results confirmed that the novel RP method can quantitatively retrieve the phase information of the investigated object. The result is comparable to that of the PS technique. Moreover, the RP approach makes highly sensitive phase tomography as simple as conventional absorption-based tomography, with an extension of sample rotation to $360°$.
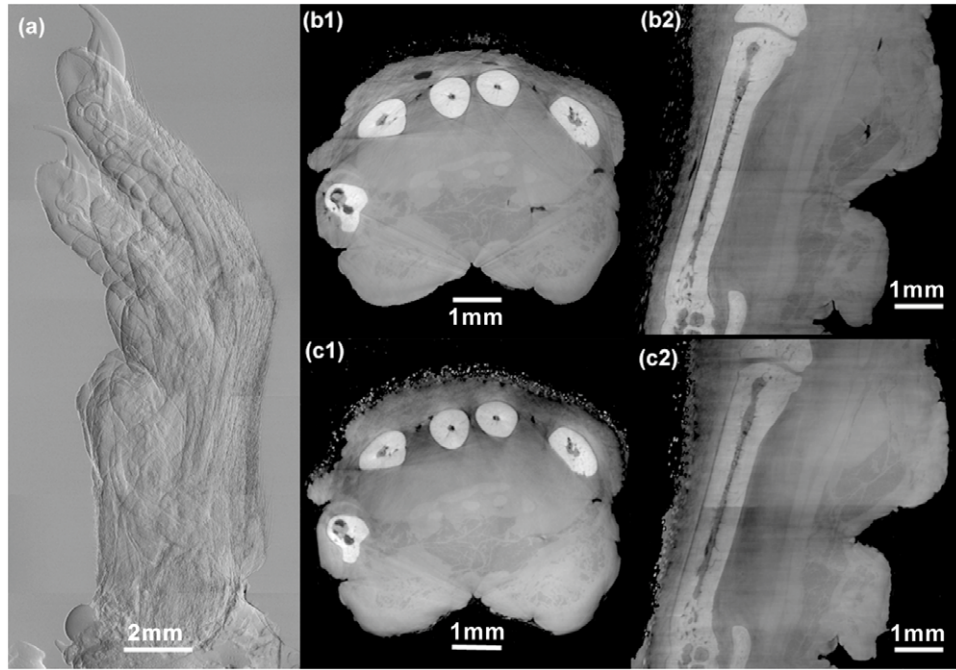
Figure 7. Imaging of a rat paw. (*a*) Differential phase-contrast radiography (seven stacks, RP method), (*b*1) axial and (*b*2) coronal slices through the rat paw acquired with the PS protocol, (*c*1) axial and (*c*2) coronal slices obtained with the RP protocol. Structural details of both soft (muscles) and hard tissues (bones) are clearly visible (Zhu *et al* 2010).

4. Discussion and conclusion

On the basis of the presented experimental results, we conclude that the proposed RP method works well in a parallel-beam geometry, i.e. either synchrotron radiation or a microfocus tube. Actually, the novel RP method can be well compatible with nonparallel beam geometries. Recently, we have discussed the generalization of the RP method to equiangular fan beam geometry using cylindrical gratings (Wu *et al* 2013). Unlike parallel beam configuration, mutual RP images in fan beam geometry are no longer automatically conjugate. By analysing the conjugate characteristic, we find that mutual reverse rays still satisfy this property. By considering rays instead of images as the unit, the paired conjugate projection images at each viewing angle can be derived. As a consequence, the absorption and refraction information can be quantitatively extracted in the fan beam configuration. More details about this topic can be found in Wu *et al* (2013). Furthermore, it has already been explained and demonstrated that the novel RP method essentially relies on a manipulation of x-ray projections, and thus its implementation on conventional x-ray sources is straightforward with a Talbot–Lau interferometer.

A comprehensive and systematic quantitative analysis of the RP method is yet not available. This will be our forthcoming work. The first issue concerns the effects of beam coherence on the performance of the RP method, especially the accuracy of the extracted information. Based on the established theoretical framework (Wang *et al* 2010a, 2010b, 2010c), we will present a detailed analysis to understand the partial coherence effects, especially on the accuracy of the RP method. On the basis of these results, we will provide an empirical formula of the range of the RP method, offering guidelines for further applications. The second issue is a quantitative description of the noise properties of the RP method both in radiography and phase tomography. This is the basis of further sensitivity analysis, and radiation dose quantification. The model will include the contributions from detector quantum noise and grating position offset, and will then be used for the quantification of several influences on the sensitivity. The noise properties will also be compared with that of conventional absorption-based imaging.

As mentioned above, a careful study of the reconstructed slices reveals that the RP protocol imposes more stringent requirements on gratings, i.e. it needs better full-field uniformity and lower local grating imperfections than gratings suitable for the PS method. In particular, imperfections may induce small ring-like artefacts in the RP-reconstructed slices, which are less evident or missing in PS reconstructions. Ring-like artefacts are clearly visible in figure 8, for both coronal (*b*1) and sagittal (*b*2) cuts. Due to the averaging effect associated with the PS extraction, the PS protocol is significantly less sensitive to grating defects and therefore the ring artefacts are less pronounced, see figures 8(*a*1) and (*a*2). Those ring-like artefacts due to grating imperfections are not present in the images of figure 5, since the field of view is relatively small ($3.58 \times 3.58\,\text{mm}^2$) and within such a small region the quality of the gratings can be considered highly homogeneous.

The recent development of grating fabrication technologies (David *et al* 2007, Noda *et al* 2008, Rutishauser *et al* 2013) has stimulated the manufacturing of optimized gratings for high x-ray energies (and therefore thicker samples), leading to the implementation of the RP protocol in new medical x-ray CT scanners that would offer a significant increase in
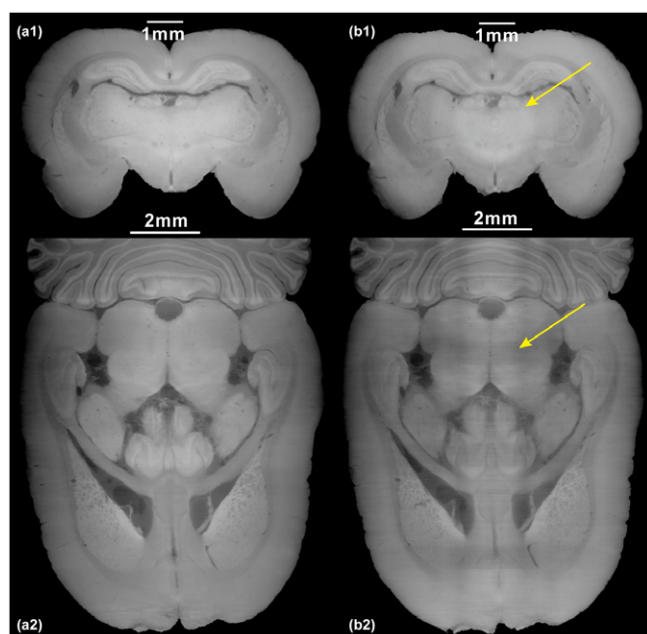
Figure 8. Tomographic reconstruction of a rat brain: (*a*1), (*a*2) obtained with the PS protocol; (*b*1), (*b*2) obtained with the RP protocol. Ring-like artefacts are clearly visible in both coronal (*b*1) and sagittal (*b*2) cuts, as indicated by the arrows.

soft tissue sensitivity. One of the future applications is the combined use of x-ray phase tomography and other medical imaging techniques. Schulz *et al* (2012) recently demonstrated that for human cerebellum, the combination of the complementary methods magnetic resonance imaging, grating-based x-ray phase tomography and histology can yield additional information on the microanatomy. The registered data with their complementary information permit the distinct segmentation of tissues within the human cerebellum.

Conclusively, it is noted that the RP approach can be performed in a single exposure, which enables the highest imaging speed (Wang *et al* 2013). And it may also be readily generalized to other imaging techniques with an identified intensity curve, such as grating-based neutron PCI (Pfeiffer *et al* 2006b) and differential interference contrast (DIC) microscopy (King *et al* 2008).

References

Arfelli F *et al* 1998 Low-dose phase contrast x-ray medical imaging *Phys. Med. Biol.* **43** 2845–52

Berujon S, Wang H, Pape I, Sawhney K, Rutishauser S and David C 2012 X-ray submicrometer phase contrast imaging with a Fresnel zone plate and a two dimensional grating interferometer *Opt. Lett.* **37** 1622–4

Bevins N, Zambelli J, Li K, Qi Z and Chen G-H 2012 Multicontrast x-ray computed tomography imaging using Talbot–Lau interferometry without phase stepping *Med. Phys.* **39** 424–8

Bonse U and Hart M 1965 An x-ray interferometer with long separated interfering beam paths *Appl. Phys. Lett.* **6** 155–6

Born M and Wolf E 1999 *Principles of Optics* 7th edn (New York: Cambridge University Press)

Chapman L D, Thomlinson W, Johnston R E, Washburn D, Pisano E, Gmur N, Zhong Z, Menk R, Arfelli F and Sayers D 1997 Diffraction enhanced x-ray imaging *Phys. Med. Biol.* **42** 2015–25

Chen G, Zambelli J, Li K, Bevins N and Qi Z 2011 Scaling law for noise variance and spatial resolution in differential phase contrast computed tomography *Med. Phys.* **38** 584–8

David C, Nöhammer B, Solak H H and Ziegler E 2002 Differential x-ray phase contrast imaging using a shearing interferometer *Appl. Phys. Lett.* **81** 3287–9

David C, Bruder J, Rohbeck T, Grunzweig C, Kottler C, Diaz A, Bunk O and Pfeiffer F 2007 Fabrication of diffraction gratings for hard x-ray phase contrast imaging *Microelectron. Eng.* **84** 1172–7

Davis T J, Gao D, Gureyev T E, Stevenson A W and Wilkins S W 1995 Phase-contrast imaging of weakly absorbing materials using hard x-rays *Nature* **373** 595–8

Donath T, Pfeiffer F, Bunk O, Grunzweig C, Hempel E, Popescu S, Vock P and David C 2010 Toward clinical x-ray phase-contrast CT demonstration of enhanced soft-tissue contrast in human specimen *Invest. Radiol.* **45** 445–52

Du Y, Liu X, Lei Y, Guo J and Niu H 2011 Non-absorption grating approach for x-ray phase contrast imaging *Opt. Express* **19** 22669–74

Ge X, Wang Z, Gao K, Zhang K, Hong Y, Wang D, Zhu Z, Zhu P and Wu Z 2011 Investigation of the partially coherent effects in a 2D Talbot interferometer *Anal. Bioanal. Chem.* **401** 865–70

Huang Z, Kang K, Zhang L, Chen Z, Ding F, Wang Z and Fang Q 2009 Alternative method for differential phase-contrast imaging with weakly coherent hard x rays *Phys. Rev.* A **79** 013815

Itoh H, Nagai K, Sato G, Yamaguchi K, Nakamura T, Kondoh T, Ouchi C, Teshima T, Setomoto Y and Den T 2011 Two-dimensional grating-based x-ray phase-contrast imaging using Fourier transform phase retrieval *Opt. Express* **19** 3339–46

King S V, Libertun A, Piestun R, Cogswell C J and Preza C 2008 Quantitative phase contrast microscopy through differential interference imaging *J. Biomed. Opt.* **13** 024020

Kohler T, Engel K J and Roessl E 2011 Noise properties of grating-based x-ray phase contrast computed tomography *Med. Phys.* **38** S106–16

Kottler C, David C, Pfeiffer F and Bunk O 2007 A two-directional approach for grating based differential phase contrast imaging using hard x-rays *Opt. Express* **15** 1175–81

Krejci F, Jakubek J and Kroupa M 2010 Hard x-ray phase contrast imaging using single absorption grating and hybrid semiconductor pixel detector *Rev. Sci. Instrum.* **81** 113702

McDonald S A, Marone F, Hintermüller C, Mikuljan G, David C, Pfeiffer F and Stampanoni M 2009 Advanced phase contrast imaging using a grating interferometer *J. Synchrotron Radiat.* **16** 562–72

Modregger P, Pinzer B R, Thüring T, Rutishauser S, David C and Stampanoni M 2011 Sensitivity of x-ray grating interferometry *Opt. Express* **19** 18324–38

Momose A and Fukuda J 1995 Phase-contrast radiographs of nonstained rat cerebellar specimen *Med. Phys.* **22** 375–9

Momose A, Takeda T, Itai Y and Hirano K 1996 Phase-contrast x-ray computed tomography for observing biological soft tissues *Nature Med.* **2** 473–5

Momose A, Kawamoto S, Koyama I, Hamaishi Y, Takai K and Suzuki Y 2003 Demonstration of x-ray Talbot interferometry *Japan. J. Appl. Phys.* **42** L866–8

Momose A, Yashiro W, Maikusa H and Takeda Y 2009 High-speed x-ray phase imaging and x-ray phase tomography with Talbot interferometer and white synchrotron radiation *Opt. Express* **17** 12540–5

Momose A, Yashiro W, Harasse S and Kuwabara H 2011 Four-dimensional x-ray phase tomography with Talbot interferometry and white synchrotron radiation: dynamic observation of a living worm *Opt. Express* **19** 8423–32

Nesterets Y I and Wilkins S W 2008 Phase-contrast imaging using a scanning-double-grating configuration *Opt. Express* **16** 5849–67

Noda D, Tanaka M, Shimada K, Yashiro W, Momose A and Hattori T 2008 Fabrication of large area diffraction grating using LIGA process *Microsyst. Technol.* **14** 1311–5

Nugent K A, Gureyev T E, Cookson D F, Paganin D and Barnea Z 1996 Quantitative phase imaging using hard x rays *Phys. Rev. Lett.* **77** 2961–4

Olivo A and Speller R 2007 A coded-aperture technique allowing x-ray phase contrast imaging with laboratory sources *Appl. Phys. Lett.* **91** 074106

Pfeiffer F, Weitkamp T, Bunk O and David C 2006a Phase retrieval and differential phase-contrast imaging with low-brilliance x-ray sources *Nature Phys.* **2** 258–61

Pfeiffer F, Grünzweig C, Bunk O, Frei G, Lehmann E and David C 2006b Neutron phase imaging and tomography *Phys. Rev. Lett.* **96** 215505

Pfeiffer F, Bunk O, David C, Bech M, Duc Le G, Bravin A and Cloetens P 2007 High-resolution brain tumor visualization using three-dimensional x-ray phase contrast tomography *Phys. Med. Biol.* **52** 6923–30

Pinzer B R, Cacquevelb M, Modreggera P, McDonaldd S A, Bensadounb J C, Thueringa T, Aebischerb P and Stampanonia M 2012 Imaging brain amyloid deposition using grating-based differential phase contrast tomography *Neuroimage* **61** 1336–46

Pisano E D *et al* 2000 Human breast cancer specimens: diffraction-enhanced imaging with histologic correlation—improved conspicuity of lesion detail compared with digital radiography *Radiology* **214** 895–901

Revol V, Kottler C, Kaufmann R, Straumann U and Urban C 2010 Noise analysis of grating-based x-ray differential phase contrast imaging *Rev. Sci. Instrum.* **81** 073709

Rizzi J, Weitkamp T, Guerineau N, Idir M, Mercere P, Druart G, Vincent G, Silva P and Primot J 2011 Quadriwave lateral shearing interferometry in an achromatic and continuously self-imaging regime for future x-ray phase imaging *Opt. Lett.* **36** 1398–400

Rutishauser S, Donath T, David C, Pfeiffer F, Marone F, Modregger P and Marco Stampanoni M 2011a A tilted grating interferometer for full vector field differential x-ray phase contrast tomography *Opt. Express* **19** 24890–6

Rutishauser S, Zanette I, Weitkamp T, Donath T and David C 2011b At-wavelength characterization of refractive x-ray lenses using a two-dimensional grating interferometer *Appl. Phys. Lett.* **99** 221104

Rutishauser S, Samoylova L, Krzywinski J, Bunk O, Grunert J, Sinn H, Cammarata M and David C 2012 Exploring the wavefront of hard x-ray free-electron laser radiation *Nature Commun.* **3** 947

Rutishauser S, Bednarzik M, Zanette I, Weitkamp T, Borner M, Mohr J and David C 2013 Fabrication of low-dimensional hard x-ray diffraction gratings *Microelectron. Eng.* **101** 12–6

Sato G *et al* 2011 Two-dimensional gratings-based phase-contrast imaging using a conventional x-ray tube *Opt. Lett.* **36** 3551–3

Schulz G *et al* 2010 High-resolution tomographic imaging of a human cerebellum: comparison of absorption and grating-based phase contrast *J. R. Soc. Interface* **7** 1665–76

Schulz G, Waschkies C, Pfeiffer F, Zanette I, Weitkamp T, David C and Muller B 2012 Multimodal imaging of human cerebellum-merging x-ray phase microtomography, magnetic resonance microscopy and histology *Sci. Rep.* **2** 826

Snigirev A, Snigireva I, Kohn V, Kuznetsov S and Schelokov I 1995 On the possibilities of x-ray phase contrast microimaging by coherent high-energy synchrotron radiation *Rev. Sci. Instrum.* **66** 5486–92

Stampanoni M *et al* 2006 Trends in synchrotron-based tomographic imaging: the SLS experience *Proc. SPIE* **6318** 63180M

Stampanoni M *et al* 2011 The first analysis and clinical evaluation of native breast tissue using differential phase-contrast mammography *Invest. Radiol.* **46** 801–6

Stutman D, Beck T J, Carrino J A and Bingham C O 2011 Talbot phase-contrast x-ray imaging for the small joints of the hand *Phys. Med. Biol.* **56** 5697–720

Suleski T 1997 Generation of Lohmann images from binary-phase Talbot array illuminators *Appl. Opt.* **36** 4686–91

Tapfer A *et al* 2012 Experimental results from a preclinical x-ray phase-contrast CT scanner *Proc. Natl Acad. Sci. USA* **109** 15691–6

Takeda M, Ina H and Kobayashi S 1982 Fourier-transform method of fringe-pattern analysis for computer-based topography and interferometry *J. Opt. Soc. Am.* **72** 156–60

Takeda Y, Yashiro W, Suzuki Y, Aoki S, Hattori T and Momose A 2007 X-ray phase imaging single phase grating *Japan. J. Appl. Phys.* **46** L89–91

Talbot H F 1836 Facts relating to optical science No. IV *Phil. Mag.* **9** 419–27

Tang X, Yang Y and Tang S 2011 Characterization of imaging performance in differential phase contrast CT compared with the conventional CT-noise power spectrum NPS(k) *Med. Phys.* **38** 4386–95

Wang D, Wang Z, Gao K, Ge X, Wu Z, Zhu P and Wu Z 2013 A dual detector approach for x-ray differential phase contrast imaging *Radiat. Phys. Chem.* DOI:10.1016/j.radphyschem.2012.12.027

Wang Z *et al* 2010a Analysis of polychromaticity effects in x-ray Talbot interferometer *Anal. Bioanal. Chem.* **397** 2137–41

Wang Z *et al* 2010b Quantitative coherence analysis with an x-ray Talbot–Lau interferometer *Anal. Bioanal. Chem.* **397** 2091–4

Wang Z *et al* 2010c Analysis of partial coherence in grating-based phase-contrast x-ray imaging *Nucl. Instrum. Methods* A **619** 319–22

Weber T, Bartl P, Bayer F, Durst J, Haas W, Michel T, Ritter A and Anton G 2011 Noise in x-ray grating-based phase-contrast imaging *Med. Phys.* **38** 4133–40

Weitkamp T, Diaz A, David C, Pfeiffer F, Stampanoni M, Cloetens P and Ziegler E 2005 X-ray phase imaging with a grating interferometer *Opt. Express* **13** 6296–304

Weitkamp T, David C, Kottler C, Bunk O and Pfeiffer F 2006 Tomography with grating interferometer at low-brilliance sources *Proc. SPIE* **6318** 63180S

Wilkins S W, Gureyev T E, Gao D, Pogany A and Stevenson W 1996 Phase-contrast imaging using polychromatic hard x-rays *Nature* **384** 335–8

J. Phys. D: Appl. Phys. **46** (2013) 494003

Z Wang *et al*

Wu Z, Gao K, Wang Z, Ge X, Chen J, Wang D, Pan Z, Zhang K, Zhu P and Wu Z 2013 A new method to retrieve phase information for equiangular fan beam differential phase contrast computed tomography *Med. Phys.* **40** 031911

Zachariasen W H 1945 *Theory of X-Ray Diffraction in Crystals* (New York: Wiley)

Zanette I, Weitkamp T, Donath T, Rutishauser S and David C 2010 Two-dimensional x-ray grating interferometer *Phys. Rev. Lett.* **105** 248102

Zhu P, Wang J, Yuan Q, Huang W, Shu H, Gao B, Hu T and Wu Z 2005 Computed tomography algorithm based on diffraction-enhanced imaging setup *Appl. Phys. Lett.* **87** 264101

Zhu P, Yuan Q, Huang W, Wang J, Shu H, Chen B, Liu Y, Li E and Wu Z 2006 Diffraction enhanced imaging: a simple model *J. Phys. D: Appl. Phys.* **39** 4142–7

Zhu P, Zhang K, Wang Z, Liu Y, Liu X, Wu Z, Mcdonald S A, Marone F and Stampanoni M 2010 Low-dose, simple, and fast grating-based x-ray phase-contrast imaging *Proc. Natl Acad. Sci. USA* **107** 13576–81